Icarus 401 (2023) 115613

Contents lists available at ScienceDirect

Icarus

journal homepage: www.elsevier.com/locate/icarus

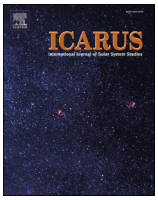

# Geological, compositional and crystallinity analysis of the Melkart impact crater, Ganymede

Alice Lucchetti [a,*], Cristina Dalle Ore [b], Maurizio Pajola [a], Riccardo Pozzobon [a], Costanza Rossi [a], Valentina Galluzzi [c], Luca Penasa [a], Katrin Stephan [d], Giovanni Munaretto [a], Gabriele Cremonese [a], Matteo Massironi [e], Pasquale Palumbo [c]

[a] INAF-OAPD Astronomical Observatory of Padova, Padova, Italy
[b] NASA Ames Research Center, Moffett Field, CA, USA
[c] INAF-IAPS, Istituto di Astrofisica e Planetologia Spaziali di Roma, Rome, Italy
[d] DLR, Berlin, Germany
[e] Geoscience Department, University of Padova, Padova, Italy

ARTICLE INFO

*Keywords:*
Ganymede
Geological processes
Ices
Jupiter, satellites
Satellites, surfaces

ABSTRACT

In this work, we analyze the ~103 km-diameter Melkart impact crater on the surface of Ganymede, which is a ~ 103 km impact crater located at the boundary between the two main geological units of the satellite, the light and dark terrains. Such crater is covered both by Galileo SSI and NIMS datasets allowing inference of any possible correlation between its geology and composition, as well as to investigate the evolution of the substrate units. We provide a geomorphological characterization of the crater by creating a high-resolution geological map, investigating the DTM and performing a strain analysis to infer its deformation. We find that the Melkart dome underwent strike-slip deformation with right-lateral kinematics. Moreover, this crater is a low strain end member with subtle deformation, which has been formed in an area of gradual transition between light and dark terrains. The results obtained through band depth and crystallinity maps of the study area do not reflect the evolutionary history of the crater, instead, they are representative of the different geological terrains affecting the subsurface of Melkart. Such result implies that the possible compositional differences between the crater's units might have been obliterated through time. Our analysis supports the interpretation that the material constituting the substrate of the crater might be heterogeneous suggesting that: (i) the transition between the two geological units might be gradual or ii) the dark material located over the study area only represents a thin layer draping the icy crust.

## 1. Introduction

The Jovian satellite Ganymede is a unique object that has been investigated in the past by both NASA Voyager 1 and 2 missions (Smith et al., 1979a, 1979b), as well as the NASA Galileo mission (Russell, 2012). The data obtained by the three spacecrafts revealed the presence of two surface units, which are different on the basis of albedo, crater density and morphology. Such units are defined as i) *dark terrain*, which is low in albedo and heavily cratered, and the ii) *light terrain*, which is characterized by fewer craters but with a higher albedo (Smith et al., 1979a, 1979b; Pappalardo et al., 2004; Patterson et al., 2010; Collins et al., 2013). Models have been proposed to explain the dark terrain crustal structure and formation suggesting that the low albedo component is mixed heterogeneously with the clean ice lithosphere of Ganymede and it is mostly concentrated as a thin layer at the surface (Prockter et al., 1998). The younger and light terrains are usually thought to be formed by the modification of the dark terrain by tectonic and possibly cryovolcanic resurfacing processes (Collins et al., 1998). It is worth mentioning that despite having different spatial densities, both units are covered by impact craters of various surface composition, sizes and morphologies, whose analysis can provide information about the impact itself, the substrate of the impact site, as well as the material involved in the impact process. Moreover, on Ganymede there are some impact craters that have been emplaced at the border of both terrains. Such features are of particular interest because they are superimposing both units, likely being formed after the light terrain formation.

* Corresponding author.
*E-mail address:* alice.lucchetti@inaf.it (A. Lucchetti).

https://doi.org/10.1016/j.icarus.2023.115613
Received 18 August 2022; Received in revised form 4 May 2023; Accepted 4 May 2023
Available online 5 May 2023

Moreover, they might reveal changes in the light terrain properties during the crater's formation when compared to the dark terrain's subsurface.

One of the best examples of these kind of impact structures is the ~103 km-size Melkart crater (10°S, 174°E), whose crater retention age is supposed to be 3.77 Gyr or 550 Myr (Stephan et al., 2003, 2008), which are derived using the lunar (Neukum et al., 1998) and outer Solar System (OSS) (Zahnle et al., 2003) chronology models, respectively. Such findings are characterized by high uncertainties due to the fact that the lunar chronology should not be easily extrapolated to the OSS, while on the other hand the knowledge of the native impact flux in the OSS is still poor. Melkart crater is partly located within the dark ancient terrain of Marius Regio and partly within the younger light grooved terrain extending from the northern Tiamat sulcus to the southern Sippar Sulcus (Fig. 1) (Patterson et al., 2010). The boundary of the two different terrains across the crater area is displayed by a linear tectonic feature transecting the crater and representing the transition between the two units (Cameron et al., 2018).

On Galileo images, Melkart crater shows a central dome which is affected by fractures and lineaments, thought to be formed by warm soft ice uplifted from several kilometers below the surface (Schenk, 2010; Hargitai and Kereszturi, 2015), hence representing the lower crust of Ganymede. In addition, an irregular depression of smooth material surrounds the dome, while the floor of the crater is both knobby and smooth (i.e. areas that may be refrozen impact melt) (Schenk, 2010).

Melkart crater represents one of the very few examples of simultaneous observations acquired by the Galileo Solid State Imaging (SSI) camera (Belton et al., 1992) with relatively high resolution (from 100 s to 10s m/px) and by the Galileo Near Infrared Mapping Spectrometer (NIMS, Carlson et al., 1992) that obtained spectra between 0.7 and 5.2 μm. In this work, we conduct an in-depth analysis of both SSI and NIMS datasets in order to study and correlate the geomorphological units with the spectral variation of the crater itself. By re-investigating such data, we prepare for the more detailed observation of this target by the future ESA JUICE mission (Grasset et al., 2013), highlighting how the correlation between different datasets is important in analyzing surface features of icy satellites. Firstly, we make use of SSI images to provide the geological characterization of Melkart crater by performing a geological map separating different units and terrains, investigating the available Digital Terrain Model (DTM) and carrying on a strain crater analysis. Then, we use NIMS data to carry out the spectral analysis by deriving both band depth and crystallinity maps of Melkart crater. We discuss our geomorphological and spectral results in order to find any correlation between the two. Finally, we conclude our work contextualizing it with the broader framework of the upcoming future space missions aiming to investigate icy satellites in general.

## 2. Dataset

We present the SSI and NIMS dataset covering the Melkart impact crater processed for this multidisciplinary analysis of the feature.

### 2.1. SSI dataset

The Galileo spacecraft acquired several images during different flybys of Ganymede, Callisto, and Europa between 1995 and 2003. The SSI camera provided images of the surface of these icy satellites in eight different broad band filters covering the 0.35–1.10 μm wavelength region and, in particular, using the clear and green filter to provide high signal-to-noise ratio (SNR) information on the geological context and surface albedo.

Among the various Galileo SSI observations, there was a dedicated acquisition of Melkart crater at higher resolution with respect to the global image mosaic of the Ganymede surface resampled at 1 km/px (Becker et al., 2001). This observation includes the following Galileo SSI frames: 2265r, 2266r, 2278r, 2279r, which are part of observation ID G8GSMELKRT01. We ingested such frames into the USGS ISIS3 image software and mosaicked them with an average resolution of 183 m. The dataset covers the latitude range of 11.9°S – 8.1°S and the longitude range of 170.5°*E*- 177.0°E. The illumination condition of the acquired observation are an incidence angle of 65°, an emission angle of 17° and a phase angle of 71°. The mosaic was georeferenced onto the Ganymede monochrome 1 km/pixel Galileo-Voyager basemap and then projected with a stereographic projection centered on Melkart crater at longitude 173.9°E and latitude 9.8°S (Fig. 2). These data provide the base for a geological map of Melkart crater and deriving a Digital Terrain Model (DTM) through the photoclinometry technique (Fig. 3) (Schenk et al., 2021).

### 2.2. NIMS dataset

Ganymede's surface was imaged by NIMS over the 0.7–5.2 μm

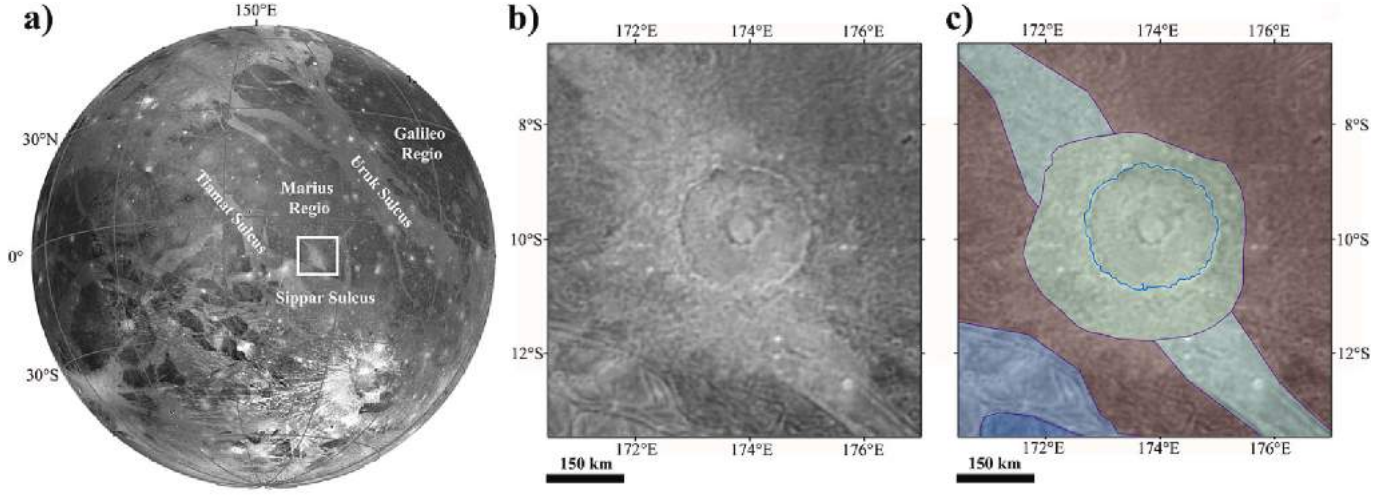


**Fig. 1.** a) Ganymede basemap (resolution of 1 km/px, Becker et al., 2001) with the location of Melkart crater indicated by the white square. b) Close up view of the Melkart impact crater: the transition between the dark and light terrain where the crater has formed is well visible in this grey scale image. c) Close up view of the geological map of Collins et al. (2013) centered on Melkart crater showing the dark terrain in brown, the light terrain in green, the geological contacts in purple and the crater rim in light-blue, respectively. At the bottom left, Sippar Sulcus light terrain is in blue. (For interpretation of the references to colour in this figure legend, the reader is referred to the web version of this article.)

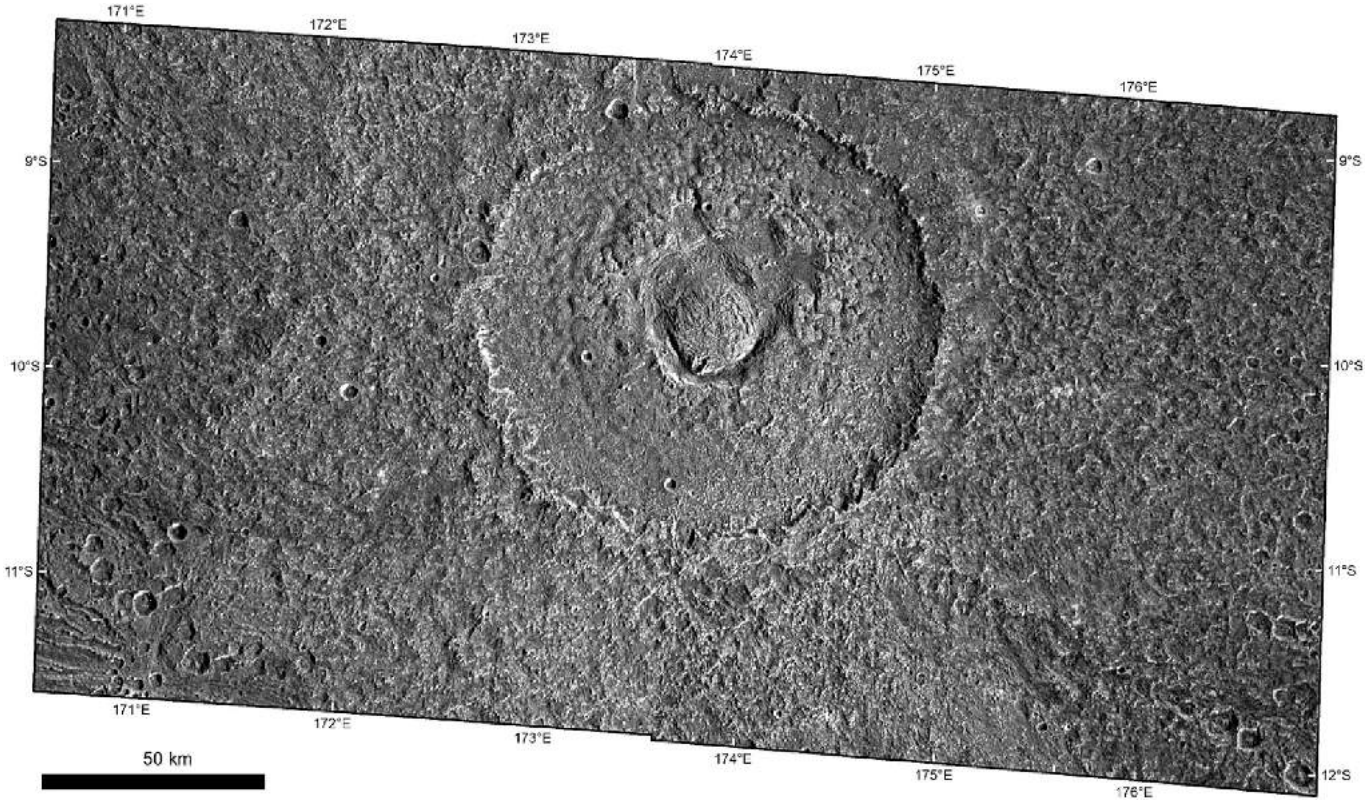


**Fig. 2.** The SSI mosaic of Melkart crater with a spatial scale of 183 m/px (G8GSMELKRT01 observation).

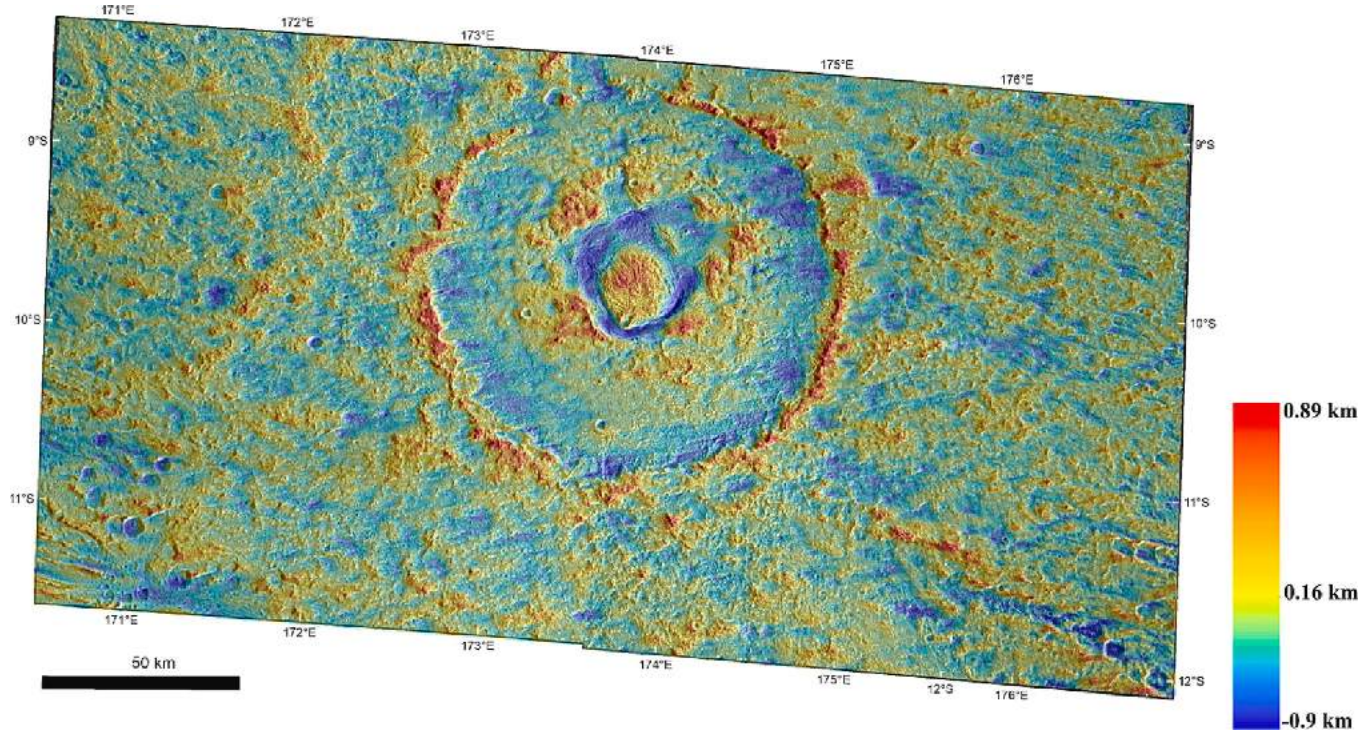


**Fig. 3.** The Digital Terrain Model of the Melkart crater obtained with the photoclinometry technique (Schenk et al., 2021).

wavelength region (Carlson et al., 1992) with a variable number of spectral channels (between 17 and 408) depending on the specific operation mode. NIMS operated as a push-broom spectrometer with a spectral resolution equal to 13 nm between 0.7 and 1 μm and to 26 nm between 1 and 5.2 μm. However, due to the extreme Jovian radiation environment, data between 1 and 1.25 μm and between 2.4 and 2.7 μm were not collected because of the failure of two detectors.

In addition to global NIMS observation of Ganymede, there were also

dedicated observations to specific targets, as the Melkart impact crater (G8GNMELKART01). Such dataset imaged the crater with a scale of 2.7 km/px at a spacecraft distance of 13,472 km and was taken with an incidence angle of 63°, emission angle of 26.1° and a phase angle of 79.6°. The cube size consists of 58 sample, 52 lines and 216 bands. Similar to the SSI mosaic, this dataset was ingested and processed in USGS ISIS3 image software to make the data usable and obtain the incidence, emission and phase angles for each pixel. Then, we used Matlab software to apply the Lommel-Seelinger photometric correction (Fairbairn, 2005) to avoid any illumination artifacts in our analysis. This is an important improvement with respect to previous NIMS localized studies where no photometric correction has ever been applied (Stephan et al., 2020). Then, we imported the dataset in ENVI software to obtain a RGB cube ($R = 2.68$ μm, $G = 1.5$ μm, $B = 0.89$ μm) and projected it onto the Melkart SSI mosaic using ESRI ArcMap software, as shown in Fig. 4.

## 3. Geomorphological mapping

We performed a geological mapping of Melkart crater based on a morphological interpretation of Galileo SSI frames described in Section 2.1. The mapping was digitized at an average scale of 1:500,000 to get the output scale shown in the map (Fig. 5). Icy terrains characterizing the mapped area were distinguished based on their morphology and surface texture.

Contacts between the units were divided into certain, where they are morphologically neat and clear, or uncertain, i.e. where approximate, gradational or subdued relationships exist between the units. For the Melkart units we introduce a new terminology based on the geomorphological appearance of the impact site. For terrains unrelated to the Melkart impact (e.g., in the south-western corner of the map) we adopt the same unit terminology provided by Collins et al. (2013).

Melkart crater is located at the western border of the dark terrain of Marius Regio and a light sulcus that branches with NW-SE direction southward from the Tiamat Sulcus to the Sippar Sulcus (Collins et al., 2013). In the geological map, the transition between the dark and light material underlying the crater is inferred based on the terrains' albedo (red dashed line in Fig. 5). We note that this transition is enhanced by a tectonic N34°W trending lineament, which crosses the eastern portion of the crater, cutting the units of the knobby floor and slightly rough floor close to its central dome (Fig. 5). Such lineament represents the southward continuation of the right-lateral fault that develops at the northern part of the sulcus, from the Tiamat Sulcus and Kishar Sulcus intersection (Cameron et al., 2018). The crosscutting of the Melkart causes a limited offset <5 km of the crater rims and a deviation of the fault orientation. In fact, two main stepover zones occur at the dome boundaries, where local extension or contraction can be accommodated (Fossen, 2010).

Within the light terrain side of the crater, we identified three different units named as slightly rough floor, moderately rough floor and knobby floor, while the dark terrain area is covered by the knobby floor material and the moderately rough floor. Morphological differences exist between the dark and light areas, and in particular, the SW portion of the knobby floor on the light terrain shows a smoother and less prominent surface than the dark one (Fig. 2). From a general perspective, the light material shows more variation on the crater floor presenting areas with different degree of roughness with respect to the dark material.

Fractures and lineaments within the Melkart central dome have been mapped and analyzed.

Azimuthal analysis has been performed for the structures on the dome (red structures in Fig. 6a), which belong to the same unit (i.e., central dome unit in Fig. 5). Wind-rose diagrams by frequency (Fig. 6b) and by length (Fig. 6c) have been produced to better characterize the orientations of the structures and better discern the main peaks that show azimuthal families. Fig. 6b shows a main NW-SE trend that is largely scattered and a secondary NE-SW trend. Such orientations are coherent with the length-weighted rose diagram in Fig. 6c, which presents a main NW-SE trend, a NE-SW trend and a third NNE-SSW trend. The spread (i.e., additional, but smaller peaks in the histogram) around the main NW-SE trend of the frequency rose diagram (Fig. 6b) allows the identification of the NNE-SSW trend in the rose by length (Fig. 6c) as azimuthal clustering, and in turn as a structural family. Therefore, we suggest the obtained trends represent three main structural families. The main NW-SE trending is consistent with the N34°W orientation of the regional shear that cuts the crater at the light/dark terrain boundary, while the second one NNE-SSW trending and a the NE-SW are consistent with synthetic and antithetic structures, subsidiary to the main shear (Fig. 6). Such orientations suggest that the crater dome underwent strike-slip deformation with right-lateral kinematics.

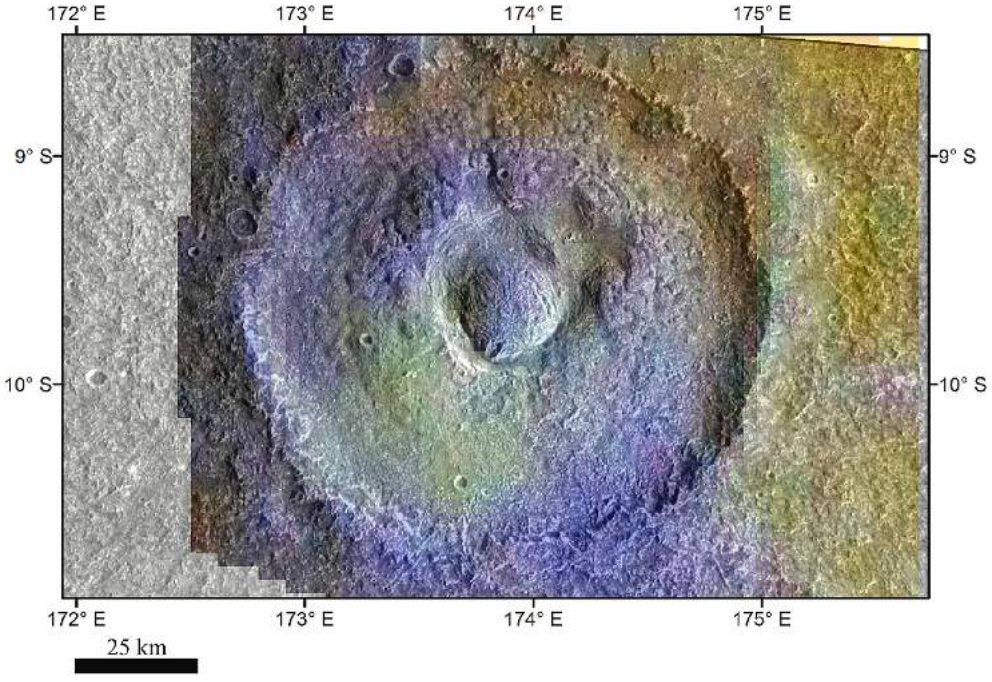


**Fig. 4.** The NIMS (G8GNMELKART01 observation) RGB false colour map (the spectral channels used for this combination is 2.68 μm for R, 1.5 μm for G and 0.89 μm for B) shows the contrast between the ice-rich light terrain (bluish colour) and the ice-poor dark terrain (yellowish colour). A peculiar green patch on the west side of the crater floor is of unknown origin and does not correlate with any observed features in Melkart (Schenk, 2010). (For interpretation of the references to colour in this figure legend, the reader is referred to the web version of this article.)

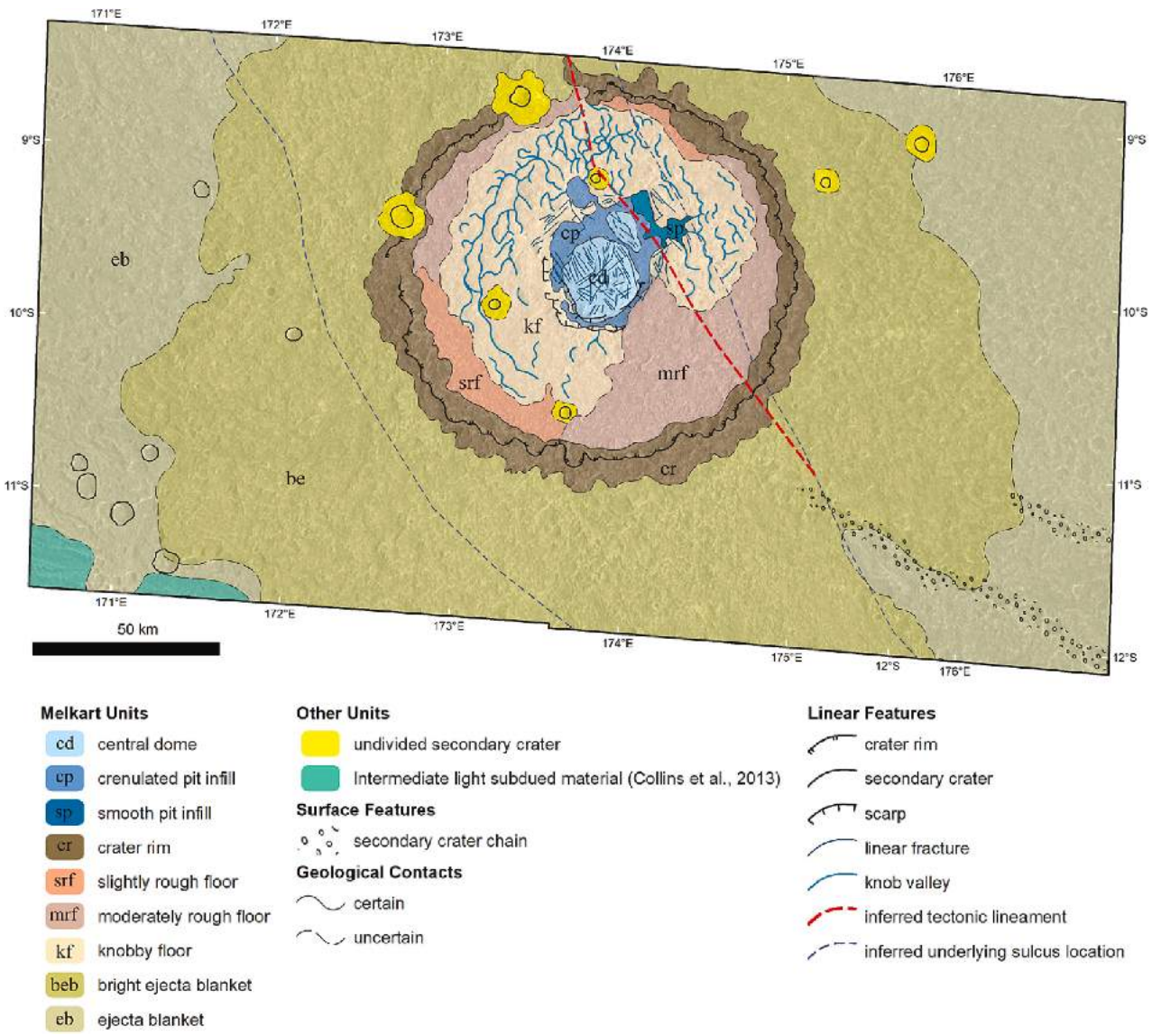


**Fig. 5.** Geological map of Melkart crater along with the legend representing the different units and features identified.

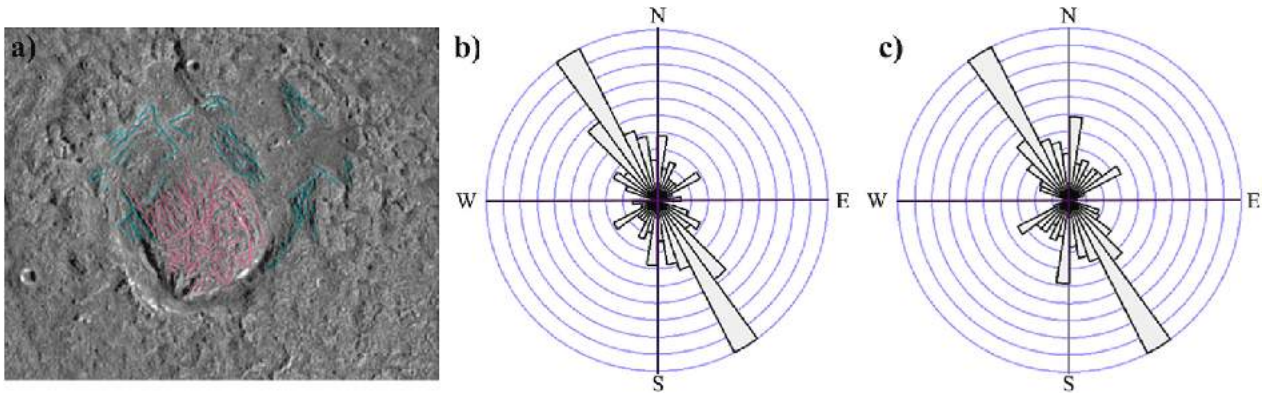


**Fig. 6.** a) The structures mapped (in red) and analyzed on the ~20 km-wide central dome of Melkart crater using the orthomosaic at 359 m/pixel, b) the rose diagram by frequency of such structures, c) the resulting length-weighted rose diagram. A total of three trends are visible: NNW-SSE, a NNE-SSW and a NE-SW. (For interpretation of the references to colour in this figure legend, the reader is referred to the web version of this article.)

From the geological analysis it is apparent that the Melkart's central pit units and central dome are off-centered and located towards the north-east of the crater floor. The knobby floor unit presents more knobs in the NNE area, along with a higher density of knob valleys (Fig. 5). This observation along with the regional-scale evidence that Melkart's distal ejecta is more extended to the NNE rather than in the other areas (Fig. 7), may be evidence for an oblique impact with NNE downrange direction.

To complete the geomorphological analysis and provide additional information on the properties of Melkart crater, we analyze the DTM obtained with the photoclinometry technique (Schenk et al., 2021) and projected onto the SSI mosaic (Fig. 8). The ratio of pit diameter to outer rim of Melkart crater is approximately 0.45, in agreement with the previous observation that the central domes on impact craters on Ganymede start to appear when such ratio exceeds 0.4 (Schenk et al., 2004). The height of the dome with respect to the depth of the pit is approximately 1–1.2 km, while its diameter is 20–25 km (Fig. 8).

## 4. Strain analysis

By means of the DTM shown in Fig. 8, we perform a crater strain analysis to infer the Melkart crater strain history by assuming a pristine circular shape, as the strain direction appears different from the impact direction (see below). On Ganymede, tectonically deformed craters can serve as markers to test the hypothesis that high-strain fault blocks can tectonically resurface pre-existing terrains (Pappalardo and Collins, 2005). Indeed, thanks to Galileo images, multiple elliptical craters have been observed on the satellite that are transected by sets of subparallel ridges and troughs oriented roughly orthogonal to the long axis of the crater, implying that these craters have been extensionally strained (Pappalardo and Collins, 2005). This is also the case of Melkart crater, which is cut by the regional-scale fault that represents the transition between dark and light terrain (Krohn et al., 2021), as shown in Fig. 5.

To perform the strain analysis, we reprojected the dataset using lambert azimuthal equal area centered on Melkart crater, as suggested in Pappalardo and Collins (2005), to get less deformation due to map projection and in order to preserve both angular and distance information around the center of the projection. Then, we extracted the rim points with a rigorous selection using the DTM and a methodology able to calculate the profile curvature with a kernel size of 11 × 11 pixels. With this approach, we calculated the amount of concavity and convexity to detect the rim slope break and map the topographic rim with higher accuracy. In Fig. 9b the concavity/convexity map is presented in blue-red scale, specifically the maximum convexity is reported in Fig. 9c, while the centroids (in cyan) of the polygonised maximum convexity are indicated in Fig. 9d. After that, we performed the strain analysis using both the methods described in Pappalardo and Collins (2005). The first method is used on strained craters clearly dislocated by a fault (i.e. the so-called *split craters*), whose offset is visible from satellite and consists in interpolating two least-square circles between the two dislocate rim portions, using as separation between the two fitting boundaries the fault visible on Galileo images. The measure of the azimuth and distance between such points gives the direction and the amount of the (brittle) deformation which involved the crater. The second method is applied on strained craters with no visible faulting, whose displacement is caused by simple shear, by fitting its rim with an ellipse and measuring the angle θ between the ellipse's major axis and the fault line, where the ellipse's major axis is equal to the amount of strain and its direction, whereas θ helps to infer the fault kinematics.

By applying the first method (i.e. the *split craters* as shown in Fig. 10a), we detected a change in the position of the circle center equal to 1705 m in WNW-ESE direction. This is less than the 2% of the average crater diameter. However, such estimation is affected by both the irregular rim and by the difference of 2539 m between the two fitting circles diameters, hence the shift in the position of the circle center can be merely the effect of the different fitting circles dimensions. The second approach consists in fitting the rim as an ellipse with semi-major axis of 104.32 km and semi-minor axis of 100.95 km, as shown in Fig. 10b, allowing the measurement of the angle between the ellipse major axis and the fault line equal to 48°. Therefore, the use of fitting ellipses shows an elongation azimuth trending ESE-WNW. Given the beforementioned qualitative impact dynamics analysis, this elongation is not consistent with the inferred impact direction. On the contrary, this is more likely consistent with a right-lateral shear and, at the same time, suggests transtentional kinematics of the fault. The low ellipticity value of the fitting ellipse, which is equal to 1.033 with ~3.5% of extension, is similar to the one of the 31 km Erichtonius crater previously studied by Pappalardo and Collins (2005) on Ganymede, which is the least deformed crater analyzed among their dataset.

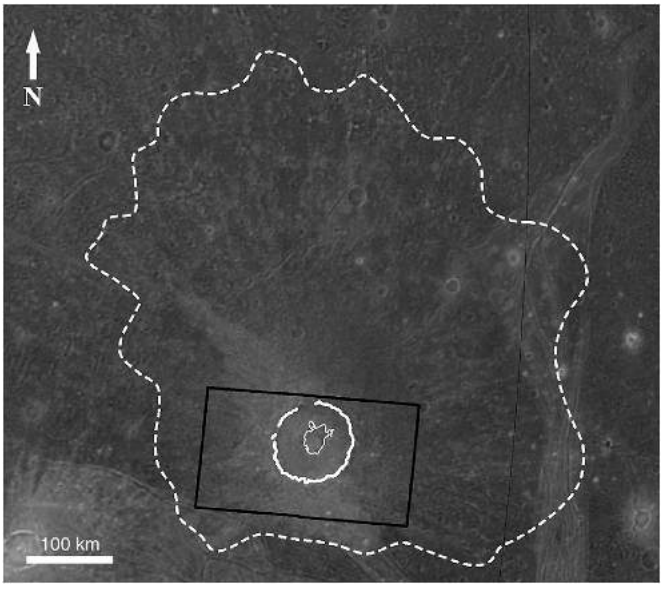


**Fig. 7.** Regional scale extent of Melkart's ejecta blanket and rays. The black outline shows the location of the SSI mosaic used in this study. The solid white outline represents Melkart's rim, and the inner pit and dome, whereas the dashed white line the approximate contact of Melkart distal ejecta. Notably, the inner pit and dome area is off-centered towards the NNE with respect to the crater's rim.

## 5. Spectral analysis

The production of band depths and, in particular, those related to the major $H_2O$-ice absorptions offers a useful indicator for the abundance and varying particle sizes in pure $H_2O$ ice (Stephan et al., 2021). Indeed, the depths of water ice diagnostic absorption features are related to both abundance and grain size (Scipioni et al., 2017): the higher the abundance, the deeper the absorption bands (for a given grain size). Likewise, larger grain sizes imply deeper absorption bands (for a given abundance). In this section, we spectrally characterize the Melkart crater using the NIMS dataset providing (i) the band depth of water ice at 1.5 and 2 μm (Carlson et al., 1996, Stephan et al., 2020) and (ii) the map of relative abundances of crystalline and amorphous ice inside and around the crater (Dalle Ore et al., 2015, 2021). Indeed, when studying impact craters on icy surfaces, the crystalline ice is used as a marker for constraining the recent emplacement of higher temperature material and can be used to determine the temporal temperature evolution of the surface (Mastrapa and Brown, 2006; Berdis et al., 2020). In particular, during a hypervelocity impact, the temperature increases inside the crater producing water ice in a crystalline form (Baragiola et al., 2013). Afterwards, the bombardment of the surface by charged particles transform such crystalline ice in a significant fraction of amorphous ice. Therefore, impacts on icy surfaces generally form water ice in the

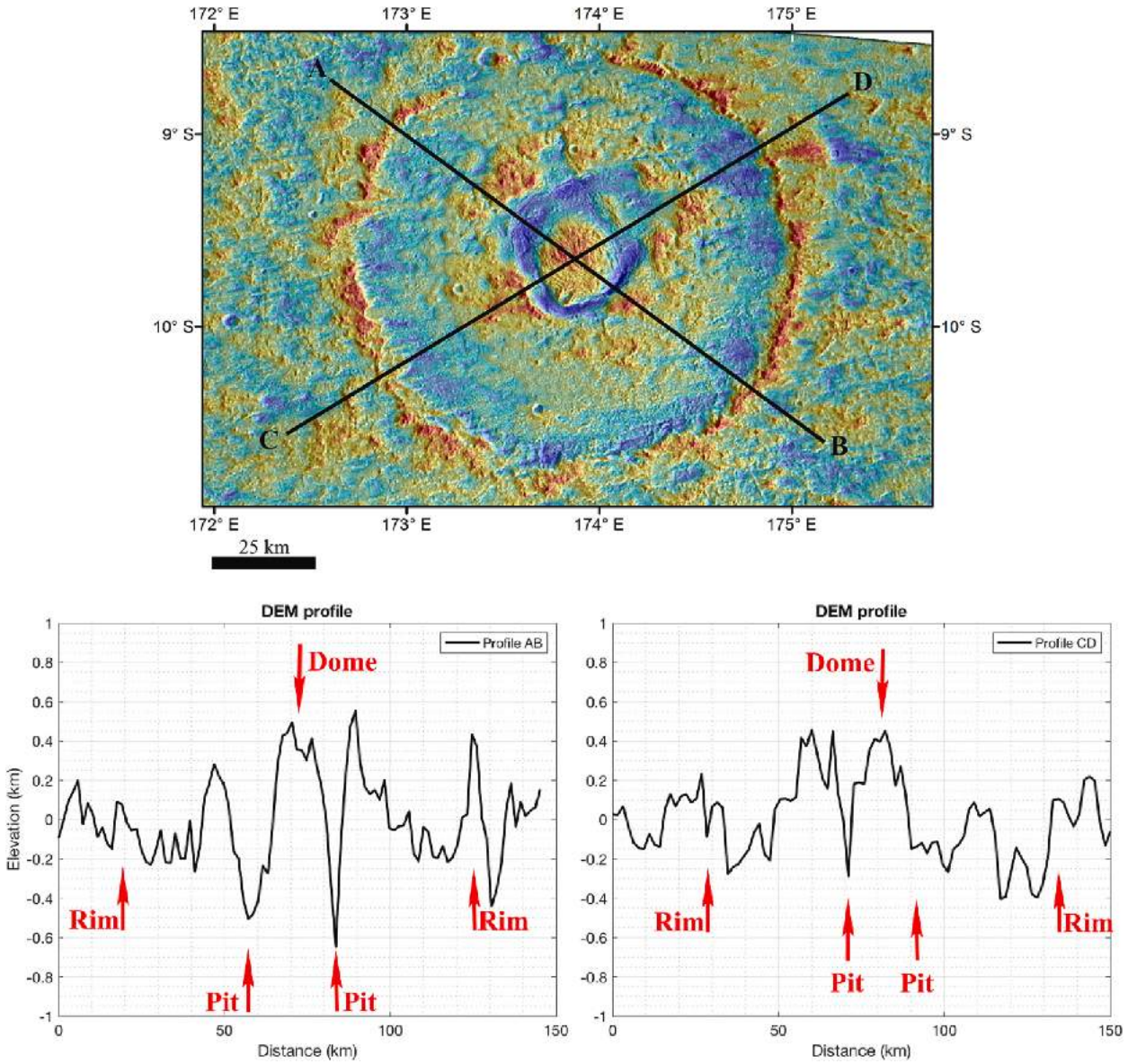


**Fig. 8.** The DTM profiles (AB and CD profiles) of the Melkart impact crater centered on the dome and the pit surrounding it.

crystalline form, which becomes amorphized by ion bombardment over time, as already demonstrated on Rhea, Dione and Europa (Dalle Ore et al., 2015, 2021; Berdis et al., 2020). In this work, we use the technique published in Dalle Ore et al. (2015) applied on Rhea's impact craters to determine the fraction of crystalline to amorphous $H_2O$ ice across the Melkart crater.

### 5.1. Water ice band depths

We consider the band depths in the IR range located at 1.5 μm and 2 μm which characterize the distribution of $H_2O$-ice in general, while the band depth at 1.25 μm cannot be investigated due to the NIMS detector failure (Stephan et al., 2020). The band depth (BD) values are defined as follows (Clark and Roush, 1984):

$$BD = 1 - (R_b/R_c)$$

Where $R_b$ is the reflectance value at the band bottom, while $R_c$ is the spectral continuum value measured at the same wavelength that is found through a linear fit between the left and right shoulders of each band. The wavelength of the NIMS spectral channels selected for the band's shoulders are: $\lambda = 1.38$ μm and $\lambda = 1.73$ μm for the 1.5 μm band and $\lambda = 1.87$ μm and $\lambda = 2.22$ μm for the 2 μm band, respectively. The produced BD(1.5) and BD(2) are reported in Fig. 11a and b, respectively.

### 5.2. Cristallinity map

To quantify the fraction of crystalline versus amorphous ice characterizing the inner and outer part of the Melkart, we follow the methodological steps that rely on the analysis of the shape of the 2 μm band. We recall that this absorption band is particularly sensitive to grain size variation, composition and temperature (Mastrapa et al., 2008) and it is commonly used to determine the ice phase changes. For a complete description of the methodology as well as the background information, we refer the reader to Dalle Ore et al. (2015, 2021).

As in Dalle Ore et al. (2015), we first applied a clustering technique to the 1.5 μm band, which is sensitive to variations in composition, grain size and temperature (Clark and Roush, 1984, Grundy and Schmitt, 1998), hence being a useful tool to discriminate among the NIMS spectra. In particular, we applied the spectral clustering technique based on a K-means algorithm, developed and evaluated by Marzo et al. (2006,

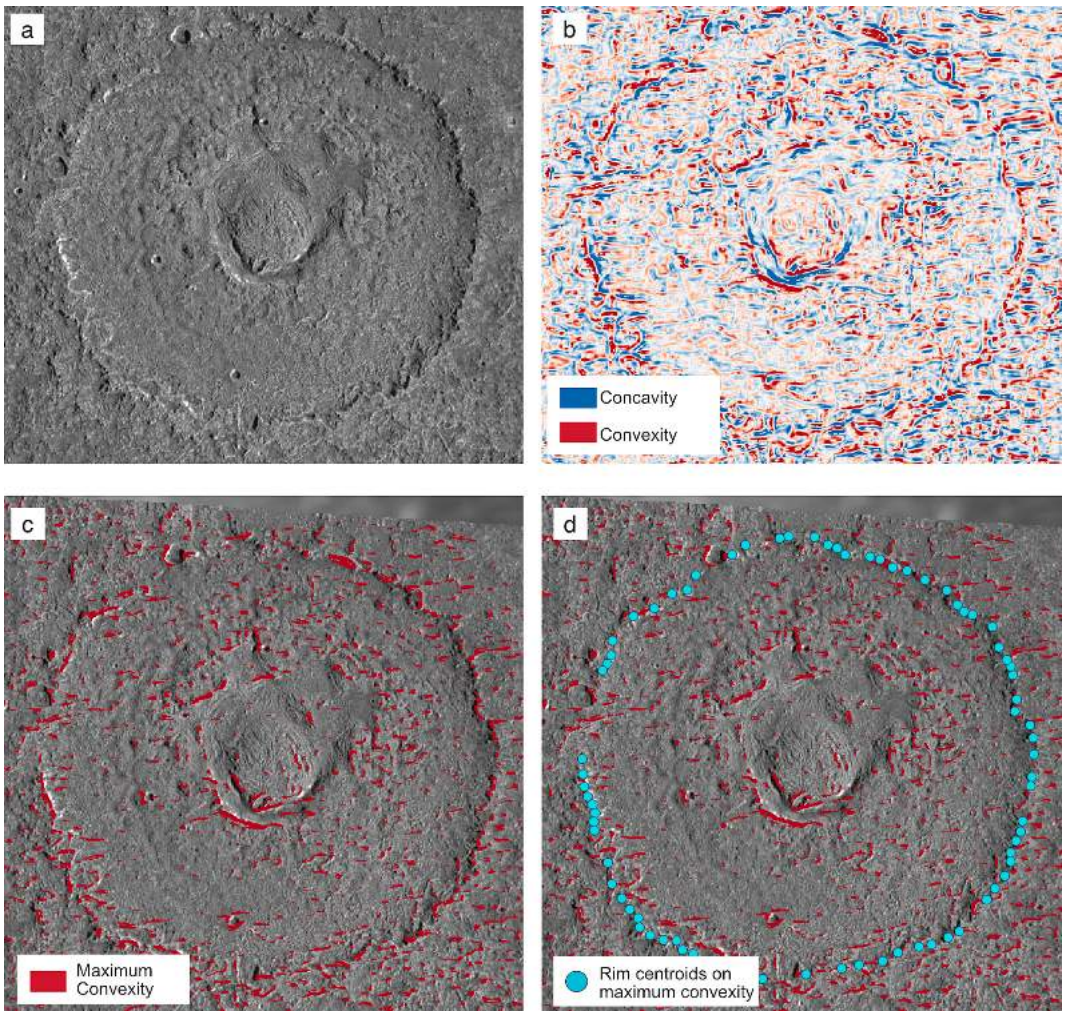


**Fig. 9.** The different phases for the Melkart crater rim points detection: a) the orthoimage from Galileo at 359 m/pixel; b) the profile curvature calculated on the photoclinometric DTM, with the concavities (blue) and convexities (red) highlighted; c) the maximum convexity map extracted in red and overlaid onto the orthoimage. The data from b) and c) were used to accurately infer the position of the points where the crater's rim is best preserved. In d) the points in cyan represent the maximum convexity and have been transformed into a point-shapefile to be used for further analysis. (For interpretation of the references to colour in this figure legend, the reader is referred to the web version of this article.)

2008, 2009), on the photometrically corrected NIMS dataset. Such approach allows to find the intrinsic number of clusters characterizing the dataset, using the Calinski-Harabasz criterion (Calinski and Harabasz, 1974). The process keeps the geographic information of each identified cluster, which is in turn characterized by an average spectrum and its associated variability, hence allowing a direct comparison between the geomorphological units and the spectral clusters. Such methodology has been already tested on other Solar System bodies, such as Mars (Marzo et al., 2006, 2008, 2009), Iapetus (Pinilla-Alonso et al., 2011; Dalle Ore et al., 2012), Rhea (Dalle Ore et al., 2015), Phobos (Pajola et al., 2018), Charon (Dalle Ore et al., 2018), Pluto (Dalle Ore et al., 2019), Dione (Dalle Ore et al., 2021) and Mercury (Lucchetti et al., 2018; Pajola et al., 2020; Lucchetti et al., 2021). The obtained cluster map and the associated average spectra are reported in Fig. 12.

For each cluster average, we model each spectrum using the Shkuratov scattering radiative transfer approach (Shkuratov et al., 1999), to determine the variations in the physical parameters. First, each model includes i) $H_2O$ ice, which is assumed to be fully crystalline, and ii) amorphous carbon (AC) that is needed to account for the darkening agent lowering the spectrum albedo. In order to correctly model our clusters' spectra we make use of $H_2O$ crystalline ice with two different grain sizes, coupled with amorphous carbon (Dalle Ore et al., 2015). We assume a temperature equal to 120 K for $H_2O$ ice in the models, in agreement with previous studies on Ganymede (Ligier et al., 2019), and adopt the optical constants for $H_2O$ ice of Mastrapa et al. (2008), and the Rouleau and Martin (1991) optical constants for the amorphous carbon. The modeling aims to match as close as possible the shape of the 2 μm band region, which is the focus of our investigation (Fig. 12c). Table 1 lists the best fitting model parameters of the components used in the models in terms of relative amounts and grain sizes.

The next step generates multiple calibration curves, as detailed in Dalle Ore et al. (2015, 2021). This consists in creating a grid of synthetic spectra starting from the best fit model and changing the relative amount of amorphous to crystalline $H_2O$ in fixed steps of ~10%. Since we consider two different components of $H_2O$ crystalline ice with different grain sizes, we initially tried to change each $H_2O$ ice component from crystalline to amorphous in order to understand what spectral variation ensues. Concerning shape and band depth, we found the spectral region around 2 μm is not sensitive to the amorphization of the $H_2O$ component characterized by larger grain sizes (1800–2500 μm). For this reason, we build the calibration curves for each cluster keeping the larger grain size $H_2O$ component crystalline and changing only the relative amount of crystalline to amorphous of the $H_2O$ component with smaller grain size. The grain size of amorphous and crystalline $H_2O$ ice is assumed to be the same.

From the synthetic spectrum associated to each cluster, we then

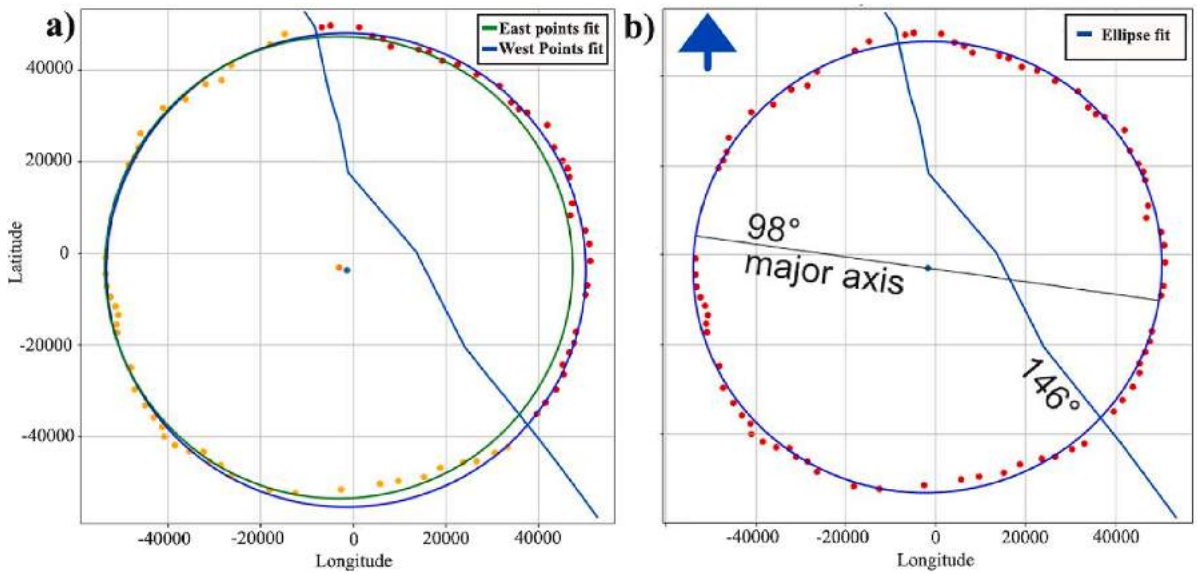


**Fig. 10.** a) Least square circles fitting method using the rim points west (red) and east (yellow) to the inferred fault line (blue polyline). The west rim points are fitted with the green least square circle, while the east points with the blue least square circle. The orange dot represents the western circle center, while the blue dot the eastern circle center. The two circles slightly differ in radius due to both the irregular shape of the crater's rim and its low preservation. Latitude and longitude are in local coordinates obtained using Lambert azimuthal projection centered on the Melkart crater's centroid, in order to minimize the deformation (as used in Pappalardo and Collins, 2005). b) Best-fitting ellipse method using all the detected Melkart rim points. The major ellipse axis and its azimuth (N82°W) are plotted together with the average fault line azimuth (N34°W). (For interpretation of the references to colour in this figure legend, the reader is referred to the web version of this article.)

calculated the "delta" value parameter (Dalle Ore et al., 2015). This is the measure of the 2 μm band asymmetry (such "delta" is also called the asymmetry parameter). Indeed, it is well known that the 1.5 μm and 2 μm bands can be fitted with a combination of Gaussians with different width and position (Grundy and Schmitt, 1998). In particular, the 1.5 μm band is composed of at least five Gaussians, while the 2 μm band is a combination of three Gaussians, among which one is predominant in its contribution to the total absorption (Grundy and Schmitt, 1998; Dalle Ore et al., 2015, 2021). Ice phase variations affect the strength of the Gaussians composing the 2 μm band (Mastrapa et al., 2008), in particular the two secondary ones, therefore affecting the change in band shape. We removed from each model the contribution of the main Gaussian by ratioing all the spectra in each grid by a Gaussian fit to the 2 μm region and measuring the difference in normalized albedo between the two minima at ~1.95 μm and ~2.1 μm (this is the so-called "delta" value). For each cluster, we derived the calibration curves connecting delta to the percentage of crystallinity for all the regions of Melkart crater, as shown in Fig. 13.

Afterwards, we measured the delta parameter for each surface pixel and associated the corresponding value of amorphous-to-crystalline fraction using the appropriate calibration curve. This was chosen based on the pixel geographic location. In Fig. 14, we report the crystallinity maps of Melkart crater with that in panel b) ranging between a maximum fraction of 75% crystalline ice to a lower limit of 50%. The majority of pixels falls within this range, while we consider the pixels with crystallinity values outside this range not statistically significant. Moreover, we highlight that we do not find a match between deltas for 8% of pixels (about 200 pixels out of 2600 pixels): this could be explained by the fact that some NIMS acquisitions can be noisy, making the analysis challenging.

## 6. Discussion

The geological map of both Melkart crater and the underlying sulcus can provide hints regarding the formation mode of the crater and its dome (Fig. 5). Indeed, the rounded central dome is characterized by the presence of fractures and lineaments as shown in Fig. 5 (Schenk, 2010), which are thought to be caused by stretching of the outer satellite's thin crust (Schenk et al., 2004). Domes on Ganymede are commonly associated with craters that usually have a diameter between 60 km and 175 km and occur within a central pit (Schenk et al., 2004). This is the case of the ~100 km-size Melkart crater, where the 20–25 km dome is clearly surrounded by an irregular depression of both crenulated (irregular) and smooth material (Fig. 5). Generally, the formation of dome is related to the post excavation stage of large impact formation and suggests a diapiric origin, whose rise began by post impact subsurface adjustments (Moore and Malin, 1988; Schenk et al., 2004). The morphology of Melkart dome and central pit fully agrees with this formation scenario.

Thanks to the DTM (Fig. 8), we geometrically characterized the Melkart crater finding that the maximum height variation between the dome and the pit is about 1–1.2 km, in agreement with the range of 0.8–1.6 km found on multiple pit dome crater on Ganymede (Schenk et al., 2004). In addition, the floor of the crater is almost flat, in accordance with low topographic variations affecting the pre-impact surface of Ganymede. The geological and strain analyses we made suggest that Melkart crater could have undergone a dextral transtentional deformation, which is also supported by the stepover of the regional fault in proximity to the dome and by the azimuthal distribution of the structures on the central dome, whose secondary peaks correspond to synthetic (the NNE-SSW trending peak) and antithetic (the NE-SW trending peak) shear. In addition, such stepover zones and brittle structures in the dome represent evidence that it is an area with different rheological response than the surroundings, consistent with its diapiric origin. Geomorphological analysis of the crater also suggests an impact direction from SSW to NNE due to the asymmetry of the ejecta blanket and the pit-dome off-centered location. Indeed, the material surrounding the crater and the abundance of the ejecta rays in the northernmost part, if compared to the southern region, could be an indicator for an oblique impact (Fig. 7). Nevertheless, a detailed ejecta study is particularly difficult due to the low resolution of the satellite global basemap.

Through a detailed DTM analysis, we have also been able to perform the strain characterization of the area, aiming to assess the Melkart deformation history (Fig. 10). Since Melkart falls at the boundary between light and dark terrains, it is more difficult to infer a strain measurement because the dark terrain should typically have undergone less or no deformation, while the well-tectonized light terrain is typically

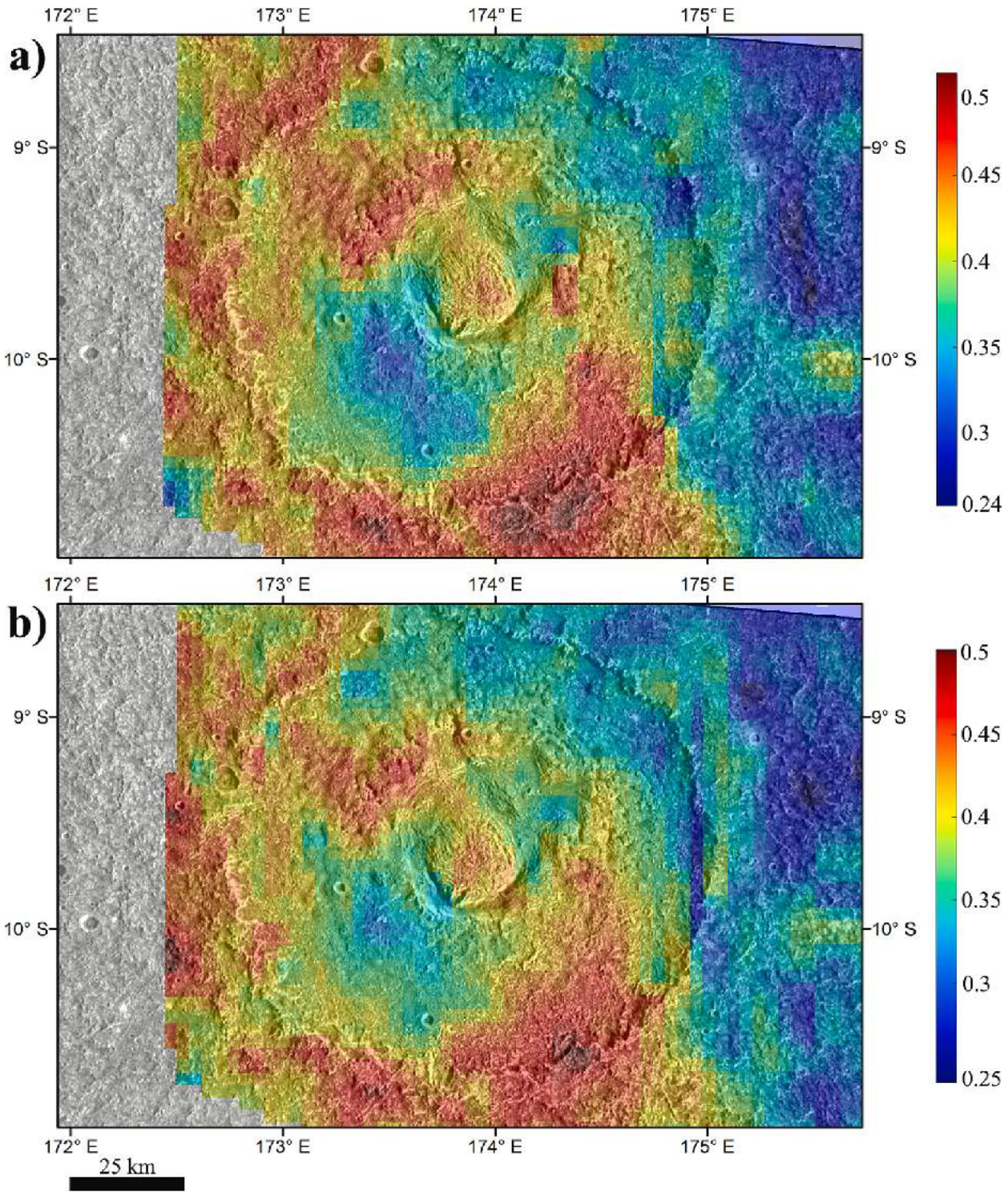


**Fig. 11.** Colour coded band depth maps of Ganymede's Melkart crater of the $H_2O$-ice absorption at (a) 1.5 μm (BD(1.5)) and (b) 2 μm (BD(2)). The BD maps are projected onto the SSI mosaic in order to correlate the spectral behavior with the geological terrains characterizing the area. The BD range values are 0.24–0.52 and 0.25–0.5, for BD(1.5) and BD(2), respectively.

fully influenced by deformation. We highlight that the presence of the NW-SE strike-slip fault may exclude a plastic deformation within the whole crater, implying a localized strain that is only partially visible. Indeed, the deformation observed in Melkart's shape is not possible to be unequivocally attributed to the fault itself.

Therefore, we suggest that Melkart is a low strain endmember with subtle deformation, which has been formed in an area of gradual transition between light and dark terrains. This is also supported by NIMS data that show that there is no strict compositional transition between the two terrains characterizing the surface of Melkart surroundings. Instead, only a patch of a terrain appears located within the light unit, which is more similar to the dark unit itself.

Melkart's deformation shows contrasting evidence that provide twofold inferences about the impact occurrence:

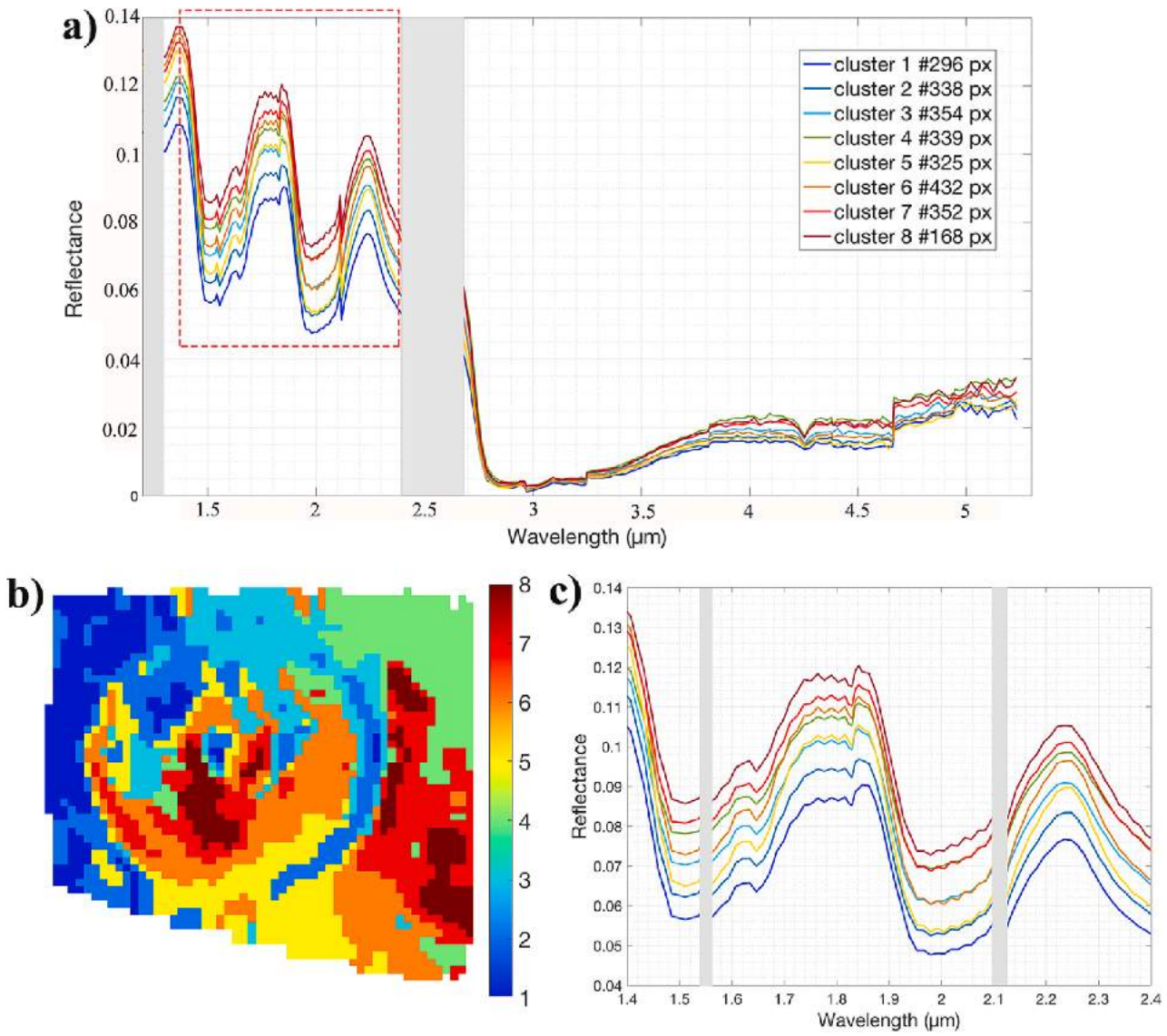


**Fig. 12.** a) Average spectra (with associated number of pixels) coming from the application of the spectral clustering technique on the 1.5 μm band. This panel shows the eight classes describing variations in grain size, composition, and temperature across the Melkart crater surface. The grey rectangles show the NIMS bad bands that are not considered in this work. b) Spatial distribution of the 8 clusters identified in the NIMS dataset. C) Close up view of panel A, in the 1.4–2.4 μm wavelength range. For A and C panels the colors of the spectra refer to the same colors used for panel B.

**Table 1**
Best-fit parameters for distinguishable mixtures composed of water ice (both crystalline and amorphous) and an AC endmember of various grain sizes.

| Region (cluster) | #1 $H_2O$ fraction (grain size in μm) | #2 $H_2O$ fraction (grain size in μm) | #3 AC fraction (grain size in μm) |
|---|---|---|---|
| 1 | 0.125 (2500) | 0.310 (29) | 0.565 (20) |
| 2 | 0.153 (1800) | 0.342 (24) | 0.505 (17) |
| 3 | 0.160 (2500) | 0.375 (17) | 0.465 (20) |
| 4 | 0.100 (2500) | 0.400 (15) | 0.500 (20) |
| 5 | 0.170 (2500) | 0.390 (24.5) | 0.450 (17) |
| 6 | 0.160 (2000) | 0.400 (19.5) | 0.440 (25) |
| 7 | 0.100 (2500) | 0.400 (15) | 0.500 (20) |
| 8 | 0.130 (2500) | 0.440 (14.5) | 0.430 (20) |

- Despite the low-resolution of the available data and all the discussed uncertainties coming from the analysis, these observations support the interpretation that the impact would likely have happened when the light terrain was in early stages of formation, i.e., when the whole terrain was gradually plastically deforming. Indeed, the light SW sector of Melkart appears particularly less tectonized and less well-developed than other light terrains nearby, such as Sippar sulcus which is located ~120 km south of Melkart itself. A possible tectonic history responsible for such deformation could be explained by the impact happening on a gradual light-dark terrain transition, where the strain was subsequently localized in a later stage along the fault.
- On the other hand, the limited offset caused by the right-lateral fault and the reduced deformation suggest that the impact occurred during the late stage of the light terrain formation, when its development was ending. In this way, the impact could possibly have remodeled the surface and has been affected by the later deformation of the underlying sulcus crosscutting the light and dark terrain boundary.

We underline that the latter hypothesis should be more probable due to the limited observed deformation of Melkart, nevertheless, both scenarios suggest that Melkart impact crater could have formed during the formation of light terrain that could have happened between 4 Gyr and 2 Gyr. Previous works suggested that Melkart crater retention age

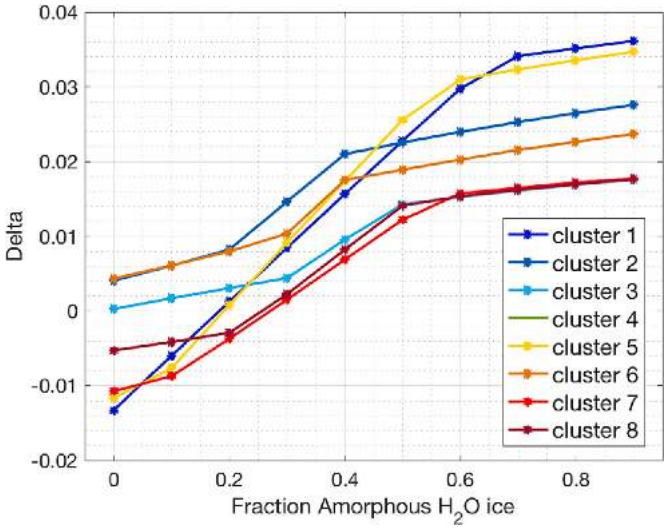


**Fig. 13.** Calibration curves for the eight regions of interest around the Melkart crater.

could be 3.77 Gyr or 550 Myr (Stephan et al., 2003) depending on the crater chronology used (Neukum et al., 1998; Zahnle et al., 2003). However, constraining the age of such a crater is really puzzling due to uncertainties of the models, such as the poor knowledge of the impact flux in the OSS. For this reason, considering our more probable tectonic formation scenario and several morphological indicators, as the small density of mapped superposed craters and the visible floor topography and ejecta, we suggest that Melkart could have an intermediate age closer to 2 Ga, and hence originated during the late stage of light terrain formation.

From the BD analysis reported in Fig. 11, we recall that the trends of the two BDs (1.5 μm and 2 μm) obtained are particularly similar. Such behavior could reflect a variation in $H_2O$ abundance with constant grain size (Stephan et al., 2020). As reported for global NIMS observations in Stephan et al. (2020), the maps variations of BD(1.5) and BD(2) are in agreement with the visible albedo variation and, hence, with the Ganymede's different geological terrains. This trend is also reflected for the Melkart study area, where low BDs values are found in correspondence with the dark material, while high BDs values are consistent with the light terrain of the underlying sulcus. The only exception is found in correspondence of the SW patch that shows a weak BD value, similar to what is observed in the dark terrain area (Fig. 11). This peculiar patch also stands out after applying the K-means spectral clustering technique and the crystallinity map is obtained. Indeed, we found a good agreement between the obtained crystallinity map and the RGB dataset reported in Fig. 4. For both maps, the patch of material located in the west part of the crater floor and the Marius Regio dark terrain located in the east part of the dataset are similar. In addition, both datasets show no variations between the crater and the dome material.

From a global perspective, the distribution of crystalline and amorphous ice on Ganymede has been previously studied in different works. Through the analysis of NIMS data, Hansen and McCord (2004) identified that the crystalline and amorphous ices form at low and high altitudes, respectively, hence suggesting that such a vertical gradient might be due to an external, charged weathering agent, such as the bombardment of charged particles orbiting inside the Jovian magnetosphere. On the contrary, by using the ground-based data obtained with the SINFONI/VLT/ESO, Ligier et al. (2019) found a very different spatial distribution: crystalline ice abundance map globally follows the same distribution trend as the abundance map of total $H_2O$-ice, while the amorphous ice appears to be distributed quite homogeneously over the surface with a light latitudinal gradient and a weak ice depletions close to the trailing hemisphere apex and at the center of Galileo Regio. The quantitative results of Ligier et al. (2019) highlighted that the crystalline ice is more distributed on the leading hemisphere of Ganymede with an abundance increase in correspondence to impact craters, while a decrease of up to 5% is observed at the equator of the trailing hemisphere. On the other hand, the abundance of amorphous ice reaches 22% at high latitudes, while it is minimal (close to 0%) both at the Galileo Regio as well as at the trailing hemisphere apex. Such results have been obtained by analyzing the global pattern of $H_2O$ ice, nevertheless, we highlight that they might not reflect the distribution at local scale owing to the much coarser spatial scale. In the Melkart crater case, which is located at 176°E, i.e. right at the edge between the leading and the trailing hemisphere, we found a crystallinity that ranges between 50% and 75% (Fig. 14). Impact crater formation generally implies the production of crystalline ice within the crater floor which with time becomes amorphous due to an infalling energetic flux of particles. So far, the Melkart crater has been considered an old crater (Stephan et al., 2008), for this reason, we would expect a distribution of ice that is more amorphous overall on the floor of the crater itself. However, we recall that the flux of charged infalling particles less affect the equatorial region of Ganymede, as reported in previous works (Ligier et al., 2019 and references therein). In addition, our geomorphological analysis may suggest that Melkart could be younger than previously reported, closer to 2 Ga which is suggested to be the late stage of light terrain formation.

From Fig. 14, we found that the area characterized by the highest crystallinity values is located in correspondence to the light terrain, while the dark terrain exhibits lower values of crystalline ice. It therefore appears that the percentage of crystalline ice might represent the different geological terrains identified (dark versus light terrains), rather

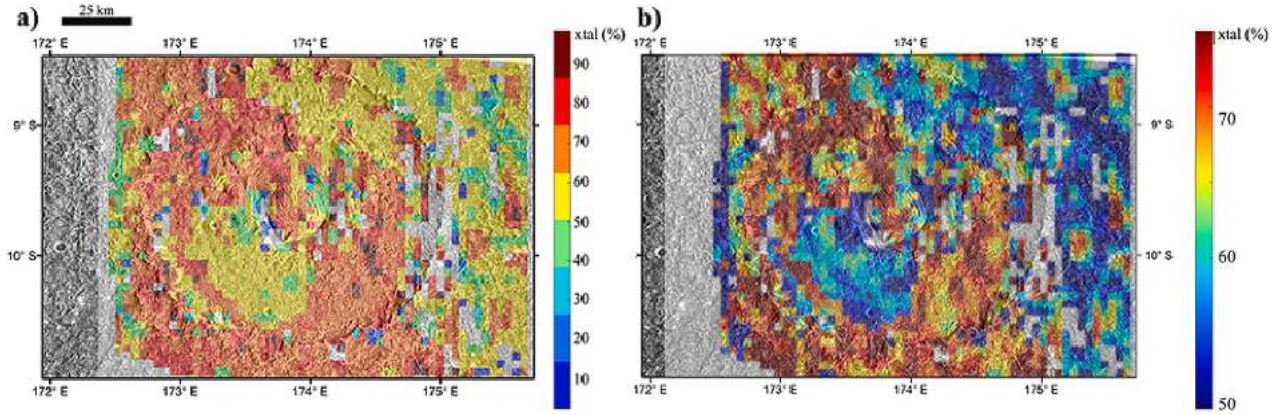


**Fig. 14.** Map of varying $H_2O$ ice phase across the Melkart crater region. a) Crystalline $H_2O$ ice map, where the legend lists the different percentages characterizing the Melkart crater overlain the SSI image; (b) Crystalline $H_2O$ ice map plotted within a crystallinity range of 50%–75% to further highlight the differences.

than the inner and outer region of the crater itself, thus not reflecting the evolutionary history of the crater. This could mean that the possible compositional differences associated with the crater have been obliterated with time and what we observe corresponds to the underlying terrains, dark and light, where the crater formed. In particular, the main crystallinity variation (25%) is not correlated with different parts of the crater: this suggests that there could be a gradual compositional transition between dark and light terrains. Though, we point out that the low quality of NIMS data could definitely affect our analysis, but the fact that there is agreement between the results obtained through different techniques supports the reliability of our findings.

Finally, we found a positive match between the geological units identified on the geomorphological map and the maps derived by applying band depths and crystallinity techniques. In particular, the SW light patch unit, which is highlighted in NIMS data as well as in band depths maps and spectral results (Fig. 11 and Fig. 14), is mainly represented by the knobby floor unit in the geological map and its location shows a surface which is smoother than the northern knobby floor (Figs. 2 and 5).

The fact that there is no strict correlation between all geological units identified and the spectral results suggests that the subsurface material constituting the Melkart location might be heterogenous, and not highlighting a strong difference in composition between the light and the dark units. In other words, we suggest that while there are two separated terrains from a morphological perspective (light and dark material which differ for the geological structures found), from a compositional perspective the first substratum of the crust is formed by material that could be a mixture of light and dark material. This is also supported by the aforementioned SW light patch that has a composition that is more similar to the dark terrain, even if it is fully located in the light terrain area. Therefore, we propose that in Melkart's location the transition between the two geological units might be gradual and/or our findings could support the interpretation that the dark material only represents a thin layer draping the icy crust (Prockter et al., 1998).

## 7. Conclusion

In this work, we performed a multidisciplinary analysis of the 100 km-size Melkart crater, which is one of the few located at the transition between the two main units of Ganymede's surface, i.e. dark and light terrains. Firstly, by making use of the Galileo/SSI dataset, we created a geological map that separated the different units and terrains present in the crater and at its closest surroundings. Such map allowed us to identify three different units (called slightly rough floor, moderately rough floor and knobby floor) in the light terrain floor and two main units (called knobby floor material and moderately rough floor) in the dark terrain floor. In addition, we examined the 20–25 km dome unit and the pit surrounding it, whose elevation and depth have been quantitatively characterized by exploiting the generated photoclinometry DTM **(Schenk et al., 2021).**

Through the azimuthal distribution analysis of the fractures and lineaments mapped on the dome we suggested that the crater dome underwent strike-slip deformation with right-lateral kinematics. The geomorphological analysis of the crater also supported an impact direction from SSW to NNE due to the asymmetry of the ejecta blanket and the pit-dome off-centered location. Melkart crater could have undergone a dextral transtentional deformation, which is also supported by the stepover of the regional fault in proximity to the dome.

Through the use of the DTM, we carried out the crater strain analysis to assess its deformation history. Such investigation supported that Melkart is a low strain end member with subtle deformation, which has been formed in an area of gradual transition between light and dark terrains. Our findings on Melkart's deformation imply that the most plausible formation scenario consists of an impact that occurred during the late stage of the light terrain formation, i.e. when its development was ending. Such event has remodeled the surface underneath, but it has been affected by the later deformation of the underlying sulcus cross-cutting the light and dark terrain boundary. If we consider the age of light terrains (from 4 to 2 Gyr) and the morphological appearance of Melkart, we may suggest that its age is closer to 2 Gyr, which is the late stage of light terrain formation.

By making use of the NIMS dataset, we performed a compositional analysis deriving the water ice band depths and the crystallinity map. The trends of the two BDs (1.5 μm and 2 μm) obtained are particularly similar, with low BDs values in correspondence to the dark material, while high BDs values are consistent with the light terrain of the underlying sulcus, in agreement with NIMS global observations on Ganymede. The only exception identified is in correspondence of the identified SW patch that shows a weak BD value, similar to what is observed in the dark terrain area. Such feature is also found in the RGB and the crystallinity maps, hence suggesting a good agreement between results obtained with different techniques. We found that the Melkart crystallinity map ranges between a maximum fraction of 75% crystalline ice to a lower limit of 50%, where higher values are in correspondence to the light terrain, while lower values correspond to the dark terrain area. We suggest such behavior does not reflect the evolutionary history of the crater since we do not observe any variation between crater units, instead it is representative of the different geological terrains affecting the subsurface of Melkart. This implies that the possible compositional differences between the area due the crater units might have been obliterated through time.

Finally, there is no strict correlation between geomorphological and spectral results, with the only exception that the light SW patch area identified in the spectral maps is represented by a knobby unit in the geological map. This could imply that the material constituting the subsurface of Melkart is heterogeneous, hence suggesting that (i) the transition between the two geological units might be gradual or ii) the dark material only represents a thin layer located over the icy crust.

Starting from the presented work, higher resolution data will be pivotal to provide an even deeper analysis of Melkart crater and icy surface features in general. Indeed, as suggested here, it is vital to analyze and correlate different datasets in order to obtain a complete overview and investigation of the processes affecting the surface of Ganymede. For this reason, re-investigating Galileo datasets is important to provide the scientific context for the observations that will be acquired by the instruments onboard the future ESA JUICE mission (Grasset et al., 2013), whose first objective will be the study of Ganymede through high resolution imagery and spectroscopy (Palumbo et al., 2014; Langevin and Piccioni, 2017). Indeed, JUICE has a comprehensive suite of remote sensing instruments that would improve the presented analysis and make new discoveries thanks to the complementary datasets that will be acquired. In particular, the JANUS camera will observe the surface of Ganymede in 12 different filters with resolutions up to 10s of meters, while the MAJIS spectrometer will shed new light on the surface composition, such as the nature of the non-ice material in terms of salts and organics, in the 0.5–5.5 wavelength region with a resolution 10 times less the JANUS camera. In addition, current datasets do not provide information about the subsurface, but thanks to RIME radar (Bruzzone and Croci, 2019) the icy crust will be explored to a maximum depth of 9 km. Moreover, data coming from the JANUS camera and GALA laser altimeter (Enya et al., 2022) will provide the 3d characterization of the overall surface improving the current knowledge of the Ganymede topography. Hence, the combination of multi- and hyper-spectral data, combined with laser altimeter and radar measurements, will be pivotal in understanding the geological processes affecting the icy surface and in revealing the correlation between surface and subsurface, which is not possible to constrain with the present space mission datasets.

## Declaration of Competing Interest

The authors declare that they have no known competing financial

interests or personal relationships that could have appeared to influence the work reported in this paper.

## Data availability

Galileo SSI and NIMS data are available through the NASA's Planetary Data System (https://pds.nasa.gov/).

## Acknowledgements

This activity has been realized under the ASI-INAF contract 2018-25-HH.0. We gratefully acknowledge funding from National Institute of Astrophysics through the INAF - Mini Grant RSN3 RIFTS project. We thank Dr. Paul Schenk for providing us the DTM used in this analysis. This work made use of the Integrated Software for Imagers and Spectrometers (ISIS), which is a product maintained by the U.S. Geological Survey Astrogeology Science Center. We made use of the ArcGIS 10.5, Matlab and IDL software to perform the presented analysis. We gratefully acknowledge the two anonymous reviewers for constructive and important comments, suggestions and corrections, that lead to a substantial improvement of the paper.

## References

Baragiola, R.A., et al., 2013. Radiation effects in water ice in the outer solar system. Sci. Solar Syst. Ices 527–549.
Becker, T., et al., 2001. Final digital global maps of Ganymede, Europa, and Callisto. Lunar Planet. Sci. Conf. XXXII, 2009.
Belton, M.J.S., et al., 1992. The Galileo solid-state imaging experiment. Space Sci. Rev. 60 (1–4), 413–455.
Berdis, J.R., Gudipati, M.S., Murphy, J.R., Chanover, N.J., 2020. Europa's surface water ice crystallinity: discrepancy between observations and thermophysical and particle flux modeling. Icarus 341, 113660.
Bruzzone, L., Croci, R., 2019, June. Radar for icy moon exploration (RIME). In: 2019 IEEE 5th International Workshop on Metrology for AeroSpace (MetroAeroSpace). IEEE, pp. 330–333.
Calinski, R.B., Harabasz, J., 1974. A dendrite method for cluster analysis. Commun. Stat. 3, 1–27.
Cameron, M.E., Smith-Konter, B.R., Burkhard, L., Collins, G.C., Seifert, F., Pappalardo, R. T., 2018. Morphological mapping of Ganymede: Investigating the role of strike-slip tectonics in the evolution of terrain types. Icarus 315, 92–114.
Carlson, R.W., Weissman, P.R., Smythe, W.D., Mahoney, J.C., 1992. Near-infrared mapping spectrometer experiment on Galileo. Galileo Mission 457–502.
Carlson, R., Smythe, W., Baines, K., Barbinis, E., Becker, K., Burns, R., et al., 1996. Near-infrared spectroscopy and spectral mapping of Jupiter and the Galilean satellites: Results from Galileo's initial orbit. Science 274 (5286), 385–388.
Clark, R.N., Roush, T.L., 1984. Reflectance spectroscopy: quantitative analysis techniques for remote sensing applications. J. Geophys. Res. Solid Earth 89 (B7), 6329–6340.
Collins, G.C., et al., 1998. Formation of Ganymede grooved terrain by sequential extensional episodes: Implications of Galileo observations for regional stratigraphy. Icarus 135 (1), 345–359.
Collins, G.C., et al., 2013. Global geologic map of Ganymede. US Department of the Interior, US Geological Survey. https://doi.org/10.3133/sim3237.
Dalle Ore, C.M., Cruikshank, D.P., Clark, R.N., 2012. Infrared spectroscopic characterization of the low-albedo materials on Iapetus. Icarus 221 (2), 735–743.
Dalle Ore, C.M., Cruikshank, D.P., Mastrapa, R.M., Lewis, E., White, O.L., 2015. Impact craters: An ice study on Rhea. Icarus 261, 80–90.
Dalle Ore, C.M., Protopapa, S., Cook, J.C., Grundy, W.M., Cruikshank, D.P., Verbiscer, A. J., et al., 2018. Ices on Charon: distribution of H2O and NH3 from New Horizons LEISA observations. Icarus 300, 21–32.
Dalle Ore, C.M., Cruikshank, D.P., Protopapa, S., Scipioni, F., McKinnon, W.B., Cook, J. C., New Horizons Surface Composition Science Theme Team, 2019. Detection of ammonia on Pluto's surface in a region of geologically recent tectonism. Sci. Adv. 5 (5), eaav5731.
Dalle Ore, C.M., Long, C.J., Nichols-Fleming, F., Scipioni, F., Valentín, E.G.R., Oquendo, A.J.L., Cruikshank, D.P., 2021. Dione's Wispy Terrain: a cryovolcanic story? Planet. Sci. J. 2 (2), 83.
Enya, K., Kobayashi, M., Kimura, J., Araki, H., Namiki, N., Noda, H., Hussmann, H., 2022. The Ganymede Laser Altimeter (GALA) for the Jupiter Icy Moons Explorer (JUICE): Mission, science, and instrumentation of its receiver modules. Adv. Space Res. 69 (5), 2283–2304.
Fairbairn, M.B., 2005. Planetary photometry: The Lommel-Seeliger law. J. R. Astron. Soc. Can. 99, 92.
Fossen, H., 2010. Structural Geology. Cambridge University Press, Cambridge, UK (463 pp.).
Grasset, O., et al., 2013. JUpiter ICy moons Explorer (JUICE): An ESA mission to orbit Ganymede and to characterise the Jupiter system. Planet. Space Sci. 78, 1–21.
Grundy, W.M., Schmitt, B., 1998. The temperature-dependent near-infrared absorption spectrum of hexagonal H2O ice. J. Geophys. Res. Planets 103, 25809–25822.
Hansen, G.B., McCord, T.B., 2004. Amorphous and crystalline ice on the Galilean satellites: A balance between thermal and radiolytic processes. Journal of Geophysical Research: Planets 109 (E1).
Hargitai, H., Kereszturi, A. (Eds.), 2015. Encyclopedia of Planetary Landforms. Springer, New York, NY, USA, pp. 1–2460.
Krohn, K., Stephan, K., Wagner, R., Baby, N.R., Schmedemann, N., 2021. Crater on Ganymede emplaced at the border of the dark and light terrain–view into the subsurface properties. EPSC 2021.
Langevin, Y., Piccioni, G., 2017. The MAJIS visible/NIR imaging spectrometer on board the ESA JUICE mission : updated design, implications for performances and science goals. Eur. Planet. Sci. Congr. v, 11.
Ligier, N., Paranicas, C., Carter, J., Poulet, F., Calvin, W.M., Nordheim, T.A., Ferellec, L., 2019. Surface composition and properties of Ganymede: Updates from ground-based observations with the near-infrared imaging spectrometer SINFONI/VLT/ESO. Icarus 333, 496–515.
Lucchetti, A., Pajola, M., Galluzzi, V., Giacomini, L., Carli, C., Cremonese, G., et al., 2018. Mercury hollows as remnants of original bedrock materials and devolatilization processes: A spectral clustering and geomorphological analysis. J. Geophys. Res. Planets 123 (9), 2365–2379. https://doi.org/10.1029/2018JE005722.
Lucchetti, A., Pajola, M., Poggiali, G., Semenzato, A., Munaretto, G., Cremonese, G., Massironi, M., 2021. Volatiles on Mercury: The case of hollows and the pyroclastic vent of Tyagaraja crater. Icarus 370, 114694.
Marzo, G.A., et al., 2006. Cluster analysis of planetary remote sensing spectral data. J. Geophys. Res. 111.
Marzo, G.A., et al., 2008. Statistical exploration and volume reduction of planetary remote sensing spectral data. J. Geophys. Res. 113.
Marzo, G.A., Roush, T.L., Hogan, R.C., 2009. Automated classification of visible and infrared spectra using cluster analysis. J. Geophys. Res. 114.
Mastrapa, R.M.E., Brown, R.H., 2006. Ion irradiation of crystalline H2O-ice: Effect on the 1.65-lm band. Icarus 183, 207–214.
Mastrapa, R.M.E., Bernstein, M.P., et al., 2008. Optical constants of amorphous and crystalline H2O-ice in the near infrared from 1.1 to 2.6 lm. Icarus 197, 307–320.
Moore, J.M., Malin, M.C., 1988. Dome craters on Ganymede. Geophys. Res. Lett. 15 (3), 225–228.
Neukum, G., Wagner, R., Wolf, U., Ivanov, B.A., Head III, J.W., Pappalardo, R.T., Galileo SSI Team, 1998, March. Cratering chronology in the jovian system and derivation of absolute ages. In: Lunar and Planetary Science Conference (No. 1742, p. 1742).
Pajola, M., Roush, T., Dalle Ore, C., Marzo, G.A., Simioni, E., 2018. Phobos MRO/CRISM visible and near-infrared (0.5–2.5 μm) spectral modeling. Planet. Space Sci. 154, 63–71.
Pajola, M., Lucchetti, A., Semenzato, A., Poggiali, G., Munaretto, G., Galluzzi, V., et al., 2020. Lermontov crater on Mercury: Geology, morphology and spectral properties of the coexisting hollows and pyroclastic deposits. Planet. Space Sci. 105136.
Palumbo, P., et al., 2014. JANUS: The Visible Camera Onboard the ESA JUICE Mission to the Jovian System. Lunar Planet. Sci. Conf. 45, 2094.
Pappalardo, R.T., Collins, G.C., 2005. Strained craters on Ganymede. J. Struct. Geol. 27 (5), 827–838.
Pappalardo, R.T., et al., 2004. Geology of Ganymede. Jupiter: Planet, Satellites, and Magnetosphere, pp. 363–396.
Patterson, G.W., et al., 2010. Global geological mapping of Ganymede. Icarus 207 (2), 845–867.
Pinilla-Alonso, N., Roush, T.L., Marzo, G.A., Cruikshank, D.P., Dalle Ore, C.M., 2011. Iapetus surface variability revealed from statistical clustering of a VIMS mosaic: The distribution of CO2. Icarus 215 (1), 75–82.
Prockter, L.M., et al., 1998. Dark terrain on Ganymede: Geological mapping and interpretation of Galileo Regio at high resolution. Icarus 135 (1), 317–344.
Rouleau, F., Martin, P.G., 1991. Shape and clustering effects on the optical properties of amorphous carbon. Astrophys. J. 377, 526–540.
Russell, C.T. (Ed.), 2012. The Galileo Mission. Springer Science & Business Media.
Schenk, P., 2010. Atlas of the Galilean satellites. Cambridge University Press.
Schenk, P.M., et al., 2004. Ages and Interiors: The cratering record of the Galilean satellites. Jupiter: The planet, satellites and magnetosphere, pp. 427–456.
Schenk, P., McKinnon, W.B., Moore, J., Nimmo, F., 2021. The Topography of Ganymede (and Callisto): Geology, Global Characteristics, and Future Exploration, 52nd Lunar and Planetary Science Conference, held virtually, 15–19 March, 2021. LPI Contribution No. 2548, id.2228.
Scipioni, F., Schenk, P., Tosi, F., D'Aversa, E., Clark, R., Combe, J.P., Dalle Ore, C.M., 2017. Deciphering sub-micron ice particles on Enceladus surface. Icarus 290, 183–200.
Shkuratov, Y., et al., 1999. A model of spectral albedo of particulate surfaces: Implications for optical properties of the Moon. Icarus 137, 235–246.
Smith, B.A., et al., 1979a. The Jupiter system through the eyes of Voyager 1. Science 204.
Smith, B.A., et al., 1979b. The Galilean satellites and Jupiter: Voyager 2 imaging science results. Science 206 (4421), 927–950.
Stephan, K., Jaumann, R., Wagner, R., Hibbitts, C.A., Hansen, G.B., 2003, March. Ganymede craters: relationships between spectral propertiesand crater retention age. In: Lunar and Planetary Science Conference, p. 1687.
Stephan, K., Wagner, R., Hibbits, C.A., Hansen, G.B., Jaumann, R., 2008. Ganymede's Impact Crater Melkart: An Example of Combination of High Resolution Spectral and Geological Analyses in the Outer Solar System. Science of Solar System Ices, Contribution, p. 9060.

Stephan, K., Hibbitts, C.A., Jaumann, R., 2020. H2O-ice particle size variations across Ganymede's and Callisto's surface. Icarus 337, 113440.

Stephan, K., Ciarniello, M., Poch, O., Schmitt, B., Haack, D., Raponi, A., 2021. VIS-NIR/SWIR spectral properties of $H_2O$ ice depending on particle size and surface temperature. Minerals 11, 1328. https://doi.org/10.3390/min11121328.

Zahnle, K., Schenk, P., Levison, H., Dones, L., 2003. Cratering rates in the outer Solar System. Icarus 163 (2), 263–289.